An International Journal of Optimization and Control: Theories & Applications
ISSN:2146-0957 eISSN:2146-5703
Vol.14, No.4, pp.378-393 (2024)
http://doi.org/10.11121/ijocta.1608

RESEARCH ARTICLE

An Inverse recursive algorithm to retrieve the shape of the inaccessible dielectric objects

Ahmet Sefer*

Department of Electrical and Electronics Engineering, FMV Işık University, Istanbul, Türkiye
ahmet.sefer@isikun.edu.tr

ARTICLE INFO

Article History:
Received 14 May 2024
Accepted 11 September 2024
Available Online 16 October 2024

Keywords:
Inverse electromagnetic scattering
Two-patch epidemic model
Electromagnetic imaging
Shape reconstruction
Surface integral equations
Newton's algorithm

AMS Classification 2010:
47A52; 47J06; 65R30; 65R32; 78A45

ABSTRACT

A regularized electromagnetic iterative inverse algorithm is formulated and implemented to reconstruct the shape of 2D dielectric objects using the far-field pattern of the scattered field data. To achieve this, an integral operator that maps the unknown boundary of the object onto the far-field pattern of the scattered field is defined and solved for the unknown boundary. The addressed inverse problem has an ill-posed nature and inherits nonlinearity. To overcome these, the proposed solution is linearized via Newton and regularized by Tikhonov in the sense of least squares. Besides, the dominance of the shadow region in the inverse-imaging process is exceeded by considering the superposition of multi-incoming plane waves, leading to less computational cost and a very fast inversion process. Comprehensive numerical analyses are carried out to ascertain the algorithm's feasibility, revealing that it is very efficient and promising.

1. Introduction

Inverse electromagnetic (EM) imaging methods that utilize scattered field data to reconstruct the shape of an unknown scatterer precisely are in significant demand across a wide variety of engineering fields, such as non-destructive testing, microwave imaging, and geophysical exploration, and so on [1–8]. Apart from its diverse applications, recovering objects from scattered fields poses an immense challenge due to its inherently nonlinear and ill-posed nature [9]. Recently, deep learning schemes and the corresponding applications have been of great interest among many engineering fields [10–12]. In addition to these, significant advancements in deep learning (DL) have led to substantial research investments in the field of inverse electromagnetic imaging problems [13–19]. In [14] and [15], the ill-posed problem is regularized considering Landweber iterations that are implemented in the regularized DL framework. [16] proposes two-step DL framework. In the first step, the dielectric properties of the inaccessible object are recovered. The object's shape is then reconstructed using the outcomes of the first step. In the sense of rough surface imaging, [18] recovers the statistical parameters of the randomly formed rough surfaces. The shape of random rough surfaces are directly recovered in [17] and [19] for different scattering scenarios.

In addition to DL applications and with the notable exception of certain non-iterative inversion techniques such as Fourier method [20], reverse time migration (RTM)-based [21] approach, and equivalent source model [22], the vast majority of algorithms developed to address these issues are based on recursive applications of regularization and linearization techniques [23–30]. Generally, these are constructed with consideration for multiple incident illuminations to enhance the precision of reconstructions [24, 25, 29, 30]. Nevertheless, these undertakings incur additional

*Corresponding Author

computational expenses. Furthermore, many of these solutions address the inverse problem associated with perfectly electric conducting (PEC) and sound-soft boundary conditions acoustically. This is because conceptually and physically, the recovery of a penetrable scatterer presents a more difficult inverse problem than the inverse problems associated with impenetrable obstacles [31]. In this regard, [29] proposes a solution to recover the 2D profile of an acoustically sound-soft scatterer by using the far-field pattern. The method utilizes multi-incidence monochromatic incident fields for illumination and applies multi-frequency measurement for higher accuracy. It solves a linearized system with a huge number of unknowns. The same consequence is valid for the linearized iterative methodologies presented in [24] and [25], which offers multi-incidence illumination for rigorous reconstructions. The principal reason for illumination is to reduce (or eliminate) the effect of shadow regions. Namely, the information in the far-field data becomes blurred for a limited amount of illumination, so the lack of information becomes dominant and yields unsuccessful reconstructions as the problem is inherently ill-posed. Alternatively, a recursive linearized method that uses only single incident illumination is proposed in [32]. The method is applied to recover unknown non-penetrable acoustically sound-soft obstacles using the far-field measured field pattern. Later, it is expanded to reconstruct the shape of penetrable objects in [26]. Within this context, for penetrable and non-penetrable cases, the far-field measured field pattern is represented by the single layer potential form [9].

This paper proposes a regularized and linearized recursive inverse algorithm to recover unknown penetrable objects using the scattered field data measured in the far-field region. Unlike other multi-illuminated inversion algorithms, the proposed algorithm applies the superposition of the multi-incident illuminations. Thus, the unknown 2D scatterer is illuminated by multiple sources simultaneously, and the scattered field is collected only once due to these simultaneous illuminations. This allows a fast inverse algorithm to obtain robust and successful reconstructions with a reduced computational cost. The superposition of incident fields is first considered for reconstructing sound-soft obstacles in [33]. Furthermore, unlike the open literature, the inverse algorithm uses a combination of double and single-layer potentials to represent the far-field measured scattered field data.

The paper's outline is provided as follows: Section 2 presents the considered EM scattering scenario, and the following Section 3 briefly summarizes the direct problem. Section 4 presents the regularized recursive inverse-imaging solution, which utilizes the far-field measurements to recover the unknown surface profile in detail. In Section 5, an extensive numerical study was conducted using various scattering scenarios to illustrate the algorithm's efficiency and examine its validation restrictions. Final remarks are given in the Section 6.

2. Geometry of the Problem

Fig. 1 represents the considered 2D scattering geometry. The unknown dielectric body is denoted as Ω embedded in infinite free space medium with permittivity ε_0 and permeability μ_0. The body is a simple non-magnetic lossy object defined in terms of constitutive electromagnetic parameters, where its permittivity and conductivity are denoted with $\varepsilon_1 = \varepsilon_0\varepsilon_r$, and σ (S/m), respectively. Accordingly, the body has a constant complex wave number k_1 with $Re\{k_1\} > 0$ and $Im\{k_1\} \geq 0$, precisely its square equals to $k_1^2 = \omega^2\varepsilon_1\mu_0 + i\omega\mu_0\sigma$, where ω is the radial operating frequency. The cross-section of the body constitutes the principle unknown of the problem, which is denoted with $\partial\Omega$ and defined as:

$$\partial\Omega := \Big\{(\rho,\varphi)\,|\,\rho = r(\varphi)\Big\}, \tag{1}$$

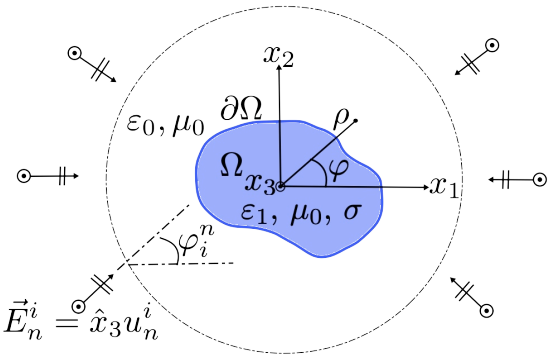

Figure 1. Geometry of the problem.

where (ρ,φ) are the cylindrical polar coordinates, such that $\rho > 0$ and $\varphi \in (0, 2\pi)$. Within this context, Ω has a star-like shape. As depicted, the 2D region is illuminated by a superposition of several monochromatic incident electric fields. The incident fields are TE polarized (transverse to wave propagation direction). The n^{th} incident is defined with a function u_n^i

$$\vec{E}_n^i = \hat{x}_3 u_n^i, \tag{2}$$

where u_n^i is the monochromatic plane wave, precisely equals

$$u_n^i = u_n^i(r(\varphi), \varphi_i^n) := e^{ik_0 r(\varphi)\cos\left(\varphi-\varphi_i^n\right)}. \quad (3)$$

Here, $k_0 > 0$ is the wavenumber of the free space. The superposition of the incident fields enables to consider the summation of incident illuminations as a single unique field, *i.e.,*

$$u^i = \sum_{n=1}^{N} u_n^i(r(\varphi), \varphi_i^n). \quad (4)$$

Regarding the incident illumination, both within the body and in the surrounding free space, the electric field vectors are in the $\hat{x}_3$ direction. Consequently, the entire problem may be simplified to a scalar one. To do so, let u_0 and u_1 denote the total fields in free space and the dielectric body, respectively. Then, both of them satisfy the scalar wave equation

$$\begin{aligned}\left(\Delta + k_0^2\right)u_0 &= 0 \text{ in } \mathbb{R}^2 \setminus \Omega,\\ \left(\Delta + k_1^2\right)u_1 &= 0 \text{ in } \Omega. \end{aligned} \quad (5)$$

Denote the derivative $r'(\varphi) = \frac{dr(\varphi)}{d\varphi}$ and the outer normal vector of $\partial\Omega$ as $\hat{\nu}$, which precisely equals

$$\hat{\nu} = \frac{\hat{\rho} r(\varphi) - \hat{\varphi} r'(\varphi)}{\sqrt{r(\varphi) + r'^2(\varphi)}}. \quad (6)$$

It follows that the fields and their derivatives with respect to the outward surface normal exhibit continuity on $\partial\Omega$. Namely, the boundary conditions imply the following:

$$u_0 = u_1, \quad (7a)$$
$$\psi_0 = \psi_1, \text{ on } \partial\Omega. \quad (7b)$$

Noting that the fields $\psi_m = \hat{\nu} \cdot \nabla u_m$ ($m = \{1, 2\}$), where "∇" denotes the gradient operator. Namely, ψ_0 and ψ_1 describe derivatives of u_0 and u_1 with respect to ν, respectively. The scattered field, in this regard, is defined as the difference

$$u^s = u_0 - u^i, \quad (8)$$

which is an outgoing wave and fulfills the Sommerfield radiation condition

$$\lim_{\rho\to\infty} \sqrt{\rho}\left(\frac{\partial u^s}{\partial \rho} - ik_0 u^s\right) = 0, \ r \text{ in } \mathbb{R}^2 \setminus \Omega \quad (9)$$

in a uniform way in all directions. Furthermore, it is straightforward to demonstrate that u^s exhibits the subsequent asymptotic behavior:

$$u^s(\rho, \varphi) = \frac{e^{ik\rho}}{\sqrt{\rho}} u_\infty(\varphi) + \mathcal{O}\left(\frac{1}{\rho^{3/2}}\right), \ \rho \to \infty. \quad (10)$$

Here, u_∞ represents the scattered field measured far away from the source, namely the far-field pattern. It is worth noting that the field also depends on k_0 and the incoming direction. However, the assumption is made by taking these quantities fixed so that u_∞ has only φ dependence. The fields defined in (7) represent the surface currents on the cross-section $\partial\Omega$. These are the unknowns of the direct scattering problem for which $\partial\Omega$ and the constitutive parameters are known. Once the currents are obtained, one can take an opportunity to obtain the fields scattered anywhere in the first medium (in our particular case, in free space). The whole procedure constitutes the "direct EM scattering problem". In the inverse problem, conversely, the inputs and the outputs are reversed. That is, the main concern is to recover the unknown cross-section, $\partial\Omega$, utilizing the measured far-field pattern of the scattered field data, *i.e.,* u_∞. To this aim, the integral representation of the scattered field data, described in the following subsection, is taken as a mapping operator into account, which maps $\partial\Omega$ onto u_∞. Hence, the problem turns into taking the inverse of the mapping operator. The following subsection describes the direct EM scattering problem applied to acquire the synthetic scattered field data utilized in the inverse problem.

3. Direct EM Problem

As mentioned above, the forward scattering problem mainly considers obtaining the surface currents given in (7) within the knowledge of the 2D cross-section $\partial\Omega$. Using Green's theorem both in the free space and Ω, one can easily obtain the integral representations of the surface currents u_0 and ψ_0 [34]

$$\begin{aligned} u_0(\boldsymbol{r}) = u^i(\boldsymbol{r}) &+ \int_{\partial\Omega} u_0(\boldsymbol{r'}) K_0(\boldsymbol{r};\boldsymbol{r'})\, ds(\varphi')\\ &- \int_{\partial\Omega} \psi_0(\boldsymbol{r'}) G_0(\boldsymbol{r};\boldsymbol{r'})\, ds(\varphi')\\ u_1(\boldsymbol{r}) = &- \int_{\partial\Omega} u_1(\boldsymbol{r'}) K_1(\boldsymbol{r};\boldsymbol{r'})\, ds(\varphi')\\ &+ \int_{\partial\Omega} \psi_1(\boldsymbol{r'}) G_1(\boldsymbol{r};\boldsymbol{r'})\, ds(\varphi') \end{aligned} \quad (11)$$

Here, $G_m(\boldsymbol{r};\boldsymbol{r'})$ ($m = \{0, 1\}$) is the fundamental solution of the scalar wave equation in 2D, *i.e.,*

$$G_m(\boldsymbol{r};\boldsymbol{r'}) = \frac{i}{4}H_0^{(1)}(k_m|\boldsymbol{r}-\boldsymbol{r'}|), \qquad (12)$$

where $\boldsymbol{r} = \hat{x}_1\rho\cos(\varphi) + \hat{x}_2\rho\sin(\varphi)$ and $\boldsymbol{r'} = \hat{x}_1 r(\varphi)\cos(\varphi') + \hat{x}_2 r(\varphi)\sin(\varphi')$ so that the argument of the Hankel-type function precisely

$$|\boldsymbol{r}-\boldsymbol{r'}| = \sqrt{\rho^2 + r^2 - 2\rho r\cos(\varphi-\varphi')}, \qquad (13)$$

and the integrand is also

$$ds(\varphi) = \sqrt{r^2 + r'^2}d\varphi. \qquad (14)$$

Noting that $r := r(\varphi)$ and $r' := r'(\varphi)$. Moreover, $K_m = \partial G_m/\partial\nu$. In regards to (8) and (11), the scattered field has an integral representation as a combination of single and double potential integral operators [9] as:

$$u^s(\boldsymbol{r}) = \int_{\partial\Omega}\Big(u_0(\boldsymbol{r'})K_0(\boldsymbol{r};\boldsymbol{r'}) - \psi_0(\boldsymbol{r'})G_0(\boldsymbol{r};\boldsymbol{r'})\Big)\,ds(\varphi'). \qquad (15)$$

Now, by substituting (7) into (11) and considering the jump relations, the subsequent classical set of the boundary integral equations are obtained [35]:

$$\begin{aligned} u^i(\boldsymbol{r}) &= \frac{1}{2}u_0(\boldsymbol{r}) - \fint_{\partial\Omega} K_0(\boldsymbol{r};\boldsymbol{r'})u_0(\boldsymbol{r'})\,ds(\varphi') \\ &\quad + \int_{\partial\Omega} G_0(\boldsymbol{r};\boldsymbol{r'})\psi_0(\boldsymbol{r'})\,ds(\varphi') \\ 0 &= -\frac{1}{2}u_0(\boldsymbol{r}) - \fint_{\partial\Omega} K_1(\boldsymbol{r};\boldsymbol{r'})u_0(\boldsymbol{r'})\,ds(\varphi') \\ &\quad + \int_{\partial\Omega} G_1(\boldsymbol{r};\boldsymbol{r'})\psi_0(\boldsymbol{r'})\,ds(\varphi'). \end{aligned} \qquad (16)$$

Accordingly, one can find the unknown surface currents by the numerical solution of the integral equations such as the method of moments (MoM) [35] and then obtain the scattered field using the integral representation given in (15). It is worth noting that the recursive inverse algorithm described in Section 4 also needs to solve the direct problem for the reconstructed shape at each iteration step. Thus, an accurate solution for the direct scattering case, for which a numerical MoM solution is applied in this study, is essential. To verify the numerical solution of the direct problem, the following subsection is designed by considering scattering from an infinite-length cylinder, which has an analytical expression in terms of the Mie series.

3.1. Validation: Scattering by dielectric cylinder

Consider an infinitely long cylinder with a cross-section radius $r = a$ located at the origin. Suppose it is a non-magnetic lossy dielectric with complex wavenumber k_1 and embedded in free space with the wavenumber k_0. An incident plane wave with the angle of incidence φ_i illuminates the cylinder. The plane wave can be expressed with the infinite Bessel series by Jacobi-Anger identity [36]:

$$\begin{aligned} u^i(r,\varphi) &= e^{ik_0 r\cos(\varphi-\varphi_i)} \\ &= \sum_{n=-\infty}^{n=+\infty} i^n J_n(k_0 r)e^{-in(\varphi-\varphi_i)} \end{aligned} \qquad (17)$$

The fields inside and outside the cylinder are denoted u_0 and u_1, respectively. They both satisfy the scalar Helmholtz equation regarding (5) and continuous on the boundary ($r = a$) as in (7). It is worth reminding that $\hat{\nu} = \hat{\rho}$ for the circular cylinder. They have series representations

$$\begin{aligned} u_0(r,\varphi) &= \sum_{n=-\infty}^{n=+\infty}\Big(B_n J_n(k_0 r) + C_n H_n^{(1)}(k_0 r)\Big)e^{-in\varphi}, \\ u_1(r,\varphi) &= \sum_{n=-\infty}^{n=+\infty} A_n J_n(k_1 r)e^{-in\varphi}, \end{aligned} \qquad (18)$$

where $B_n = i^n e^{in\varphi_i}$ according to (17). Substituting (18) into (7) yields

$$\begin{aligned} B_n J_n(k_0 a) + C_n H_n^{(1)}(k_0 a) &= A_n J_n(k_1 a) \\ B_n J_n'(k_0 a) + C_n H_n'^{(1)}(k_0 a) &= \frac{k_1}{k_0}A_n J_n'(k_1 a). \end{aligned} \qquad (19)$$

Leading with $\varsigma = k_1/k_0$, the solution reads:

$$\begin{aligned} A_n &= B_n\frac{H_n^{(1)}(k_0 a)J_n'(k_0 a) - H_n'^{(1)}(k_0 a)J_n(k_0 a)}{\varsigma H_n^{(1)}(k_0 a)J_n'(k_1 a) - H_n'^{(1)}(k_0 a)J_n(k_1 a)}, \\ C_n &= B_n\frac{J_n(k_1 a)J_n'(k_0 a) - \varsigma J_n(k_0 a)J_n'(k_1 a)}{\varsigma H_n^{(1)}(k_0 a)J_n'(k_1 a) - H_n'^{(1)}(k_0 a)J_n(k_1 a)}. \end{aligned} \qquad (20)$$

Accordingly, one can compute the total fields inside and outside the cylinder by substituting (20) into (18). In the context of the numerical MoM-point matching solution, the whole cylinder sampled as follows: The circular cylinder with radius $r(\varphi) = a$ has a circumference $2\pi a$ with $0 \le \varphi < 2\pi$İt is divided into the number of N equally spaced segments. n^{th} segment is denoted φ_n with its width is $\Delta\varphi$, precisely

$$\varphi_n = (n-1)\Delta\varphi \text{ with } \Delta\varphi = \frac{2\pi}{N}. \tag{21}$$

Here, $n \in [1,\ N]$ and the sample number is settled as

$$N = 10\left|\frac{k_1}{k_0}\right|2\pi a \tag{22}$$

The unknown surface fields in (16) are expanded as linear combinations of the pulse-basis subdomain functions with some unknown coefficients positioned at each segment's center. Namely,

$$\begin{Bmatrix} u_0 \\ \psi_0 \end{Bmatrix} \approx \sum_{n=1}^{N} \begin{Bmatrix} u_n \\ \psi_n \end{Bmatrix} f_n(\varphi), \tag{23}$$

where the pulse basis function,

$$f_n(\varphi) = \begin{cases} 1 & (\varphi_n - \Delta\varphi/2) \le \varphi \le (\varphi_n + \Delta\varphi/2) \\ 0 & \text{elsewhere .} \end{cases} \tag{24}$$

The length of each segment is sufficiently small so that the integrand doesn't vary significantly. Regarding point matching, the whole equation is weighted by Dirac-delta functions. Accordingly, one can obtain the matrix equation system.

$$\overline{\overline{Z}}_{die}\,\overline{I}_{die} = \overline{V}_{die}, \tag{25}$$

where $\overline{I}_{die}$ and $\overline{V}_{die}$ are vectors with size $2N \times 1$. The elements of the vectors and the impedance matrices are precisely given in the appendix. The numerical comparison of the analytic and MoM solutions for a dielectric cylinder is given in the following subsection.

3.2. Numerical comparisons for a dielectric cylinder

To validate MoM-point matching with the analytic Mie series solution, a dielectric lossy cylinder with radius $r = 2$m is considered. Outside of the cylinder is free space, and the dielectric parameters are $\varepsilon_r = 4$ and $\sigma = 5 \times 10^{-5}$. In (18), $n = 64$ and in (22), $N = 252$. Operating frequency is 300 MHz, the angle of the incident plane wave illumination $\varphi = 60°$. The following figures 2 and 3 show the modulus and the phase of the surface fields acquired by MoM and analytic series, respectively.

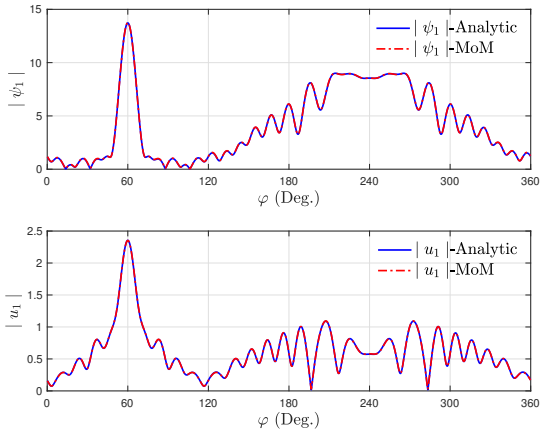

Figure 2. Modulus of the surface fields on dielectric cylinder

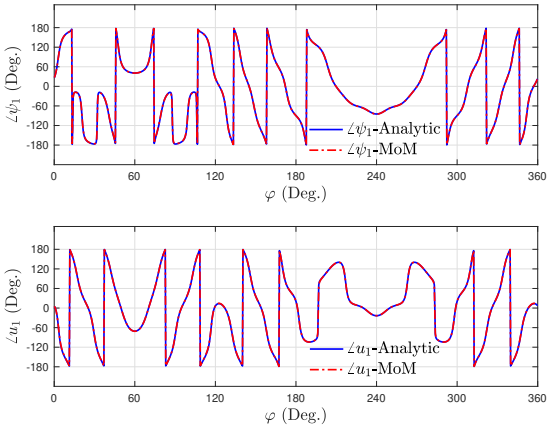

Figure 3. phase of the surface fields on dielectric cylinder

To compare the results quantitatively, an ℓ_2 norm-based error is defined between the fields obtained from analytic and MoM solutions:

$$e(\%) = \frac{\|u_{\mathrm{A}} - u_{\mathrm{MoM}}\|_2}{\|u_{\mathrm{A}}\|_2} \times 100. \tag{26}$$

Here, u_{A} and u_{MoM} denote the surface fields obtained by analytic and MoM solutions, respectively. The obtained surface fields with MoM solution in the figures 2 and 3 requires sampling $N = 252$. High agreements were achieved between the MoM and analytical solutions. The numerical errors obtained for this sampling number are below 2% for both u_0 and ψ_0. As expected, increasing the number of samples in MoM improves the agreement between the two methods. Hence, the quantitative error decreases for a higher sampling number. The obtained errors for increased N values are shown in Fig. 4

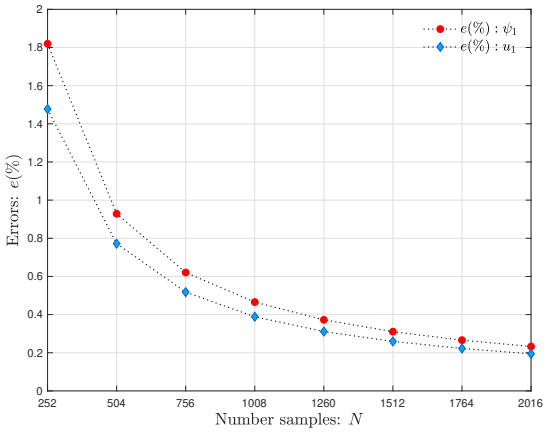

Figure 4. Errors vs. the number of samples in MoM

4. Inverse Problem

The inverse problem addressing involves determining the boundary $\partial\Omega$ of the scatterer Ω, given the far-field pattern u_∞ for the superposition of the incident plane wave illuminations u^i. To define the far-field pattern precisely, it is necessary to consider the asymptotic behavior of the Hankel type functions for large argument, which equals [36]

$$H_0^{(1)}(\omega) = \sqrt{\frac{2}{\pi\omega}} e^{i\omega - \frac{\pi}{4}} \left(1 + \mathcal{O}\left(\frac{1}{\omega}\right)\right), \omega \to \infty. \tag{27}$$

Within this context, assume that a point in the far field is described as $\boldsymbol{r_s} := r_s(\hat{x}_1 \cos(\varphi_s) + \hat{x}_2 \sin(\varphi_s))$ and the cross-section is represented as in (1). Then, in accordance with Huygens' principle [37], the standard approximation for the 2D Green's function given in (12) and (13) have the phase term and the amplitude term as following

$$\tilde{G}(\boldsymbol{r}; \boldsymbol{r_s}) = \gamma e^{ik_0 r_s} e^{-ik_0 r(\varphi)\cos(\varphi_s - \varphi)}, \tag{28}$$

where the constant

$$\gamma = \frac{i}{4}\sqrt{\frac{2}{\pi k_0 r_s}} e^{-i\frac{\pi}{4}}. \tag{29}$$

That is, the modulus term of $\tilde{G}$ is approximated as $|\boldsymbol{r} - \boldsymbol{r_s}| \approx r_s$ and the phase term is $|\boldsymbol{r} - \boldsymbol{r_s}| \approx r_s - k_0(\boldsymbol{r_s} \cdot \boldsymbol{r})$. It is naturally a good approximation for Green's functions and is conventionally applied to represent a far-field pattern of the scattered field. The reader may refer to [38] for the Huygens' principle in 3D and 2D scattering problems [39], for the details of the far-field expansion of 2D Green's function, and thus the far-field expansion of the Greens' function [34, 37]. In this context, one can easily define the derivative of the function with respect to the surface normal $\hat{\nu}$ as

$$\frac{\partial \tilde{G}(\boldsymbol{r}; \boldsymbol{r_s})}{\partial \nu} = \hat{\nu} \cdot \nabla \tilde{G}(\boldsymbol{r}; \boldsymbol{r_s}) = -i\tilde{G}(\boldsymbol{r}; \boldsymbol{r_s})\hat{k}_s \cdot \hat{\nu}. \tag{30}$$

Here, $\hat{k}_s$ is the wavenumber vector in scattering direction with the angle φ_s, particularly equals to

$$\hat{k}_s = k_0\Big(\hat{x}_1 \cos(\varphi_s) + \hat{x}_2 \sin(\varphi_s)\Big), \tag{31}$$

which can be converted into polar coordinates:

$$\hat{k}_s = k_0\Big(\hat{\rho} \cos(\varphi_s - \varphi) + \hat{\varphi} \sin(\varphi_s - \varphi)\Big). \tag{32}$$

Accordingly, the far-field scattered field has the integral representation as

$$u_\infty(\varphi) = \gamma \int_{\partial\Omega} \Big(- i\hat{k}_s \cdot \hat{\nu} u_0(\varphi') + \psi_0(\varphi') \Big) e^{-ik_0 r(\varphi')\cos(\varphi_s - \varphi')}\, ds(\varphi'). \tag{33}$$

Substituting (6) and (31) into (33) yields more precise expression for u_∞ as

$$\begin{aligned} u_\infty(\varphi) = -ik_0\gamma \int_0^{2\pi} \Big\{ \Big(& r(\varphi')\cos(\varphi_s - \varphi') \\ & - r'(\varphi')\sin(\varphi_s - \varphi') \Big) u_0(\varphi') \\ & + \psi_0(\varphi') \sqrt{r(\varphi')^2 + r'(\varphi')^2} \Big\} \\ & e^{-ik_0 r(\varphi')\cos(\varphi_s - \varphi')}\, d\varphi'. \end{aligned} \tag{34}$$

To have a much more compact form of (34), the integral equation can be defined in an operator form $\mathcal{D}$. Thus, with the knowledge of the u_∞ and the surface fields, the inverse problem consists of solving the nonlinear and ill-posed equation

$$\mathcal{D}(r, u_0, \psi_0) = u_\infty, \tag{35}$$

for the unknown boundary $\partial\Omega$ represented by $r := r(\varphi)$. To start with the inversion process, first, the operator is linearized via Newton's type iterations and then regularized by Tikhonov. Within the context of linearization, let r_0 be the initially guessed shape, for which one can solve the direct problem to obtain the surface currents (u_{1_0}, ψ_{1_0}) of the guessed shape. Accordingly, the linearization proceeds in the sense of Newton as

$$\mathcal{D}(r,u_0,\psi_0)\approx\mathcal{D}(r_0,u_{0_0},\psi_{0_0})+\mathcal{D}'(r_0;u_{0_0},\psi_{0_0})\delta r_0. \tag{36}$$

Here, $\mathcal{D}'(r_0;u_{1_0},\psi_{1_0})\delta r_0$ is the Frechet derivative of the surface with respect to r, and δr_0 is the updated correlation function for which (36) has to be solved. For the regularization procedure, let $\mathcal{D}_0'$ stand for the Frechet derivative for a short notation, and its ad-joint be denoted by $\mathcal{D}_0'^{\dagger}$. Then, by defining a regularization parameter $0<\tau<1$, δr_0 is the solution of

$$\tau\delta r_0+\mathcal{D}_0'^{\dagger}\mathcal{D}_0'=\mathcal{D}_0'^{\dagger}\Delta u_\infty, \tag{37}$$

where $\Delta u_\infty=u_\infty-\mathcal{D}(r_0,u_{1_0},\psi_{1_0})$. Furthermore, one may also consider a scaling (tuning) parameter to have a much more robust δr_0. In this sense, the solution of (37) is written as

$$\delta r_0=\alpha\big[\tau\mathbf{I}+\mathcal{D}_0'^{\dagger}\mathcal{D}_0'\big]^{-1}\mathcal{D}_0'^{\dagger}\Delta u_\infty. \tag{38}$$

Here, $\mathbf{I}$ is the identity matrix, and $0<\alpha<1$ is the scaling parameter. The reader may refer to [40] for the details of α and τ. For a predetermined threshold ξ, the procedure is repeated recursively until the stopping criteria $\|\delta r_N\|_2\leq\xi$. Accordingly, n^{th} approximated boundary is updated by setting

$$r_{n+1}=r_n+\delta r_n. \tag{39}$$

Moreover, to have a more robust reconstruction, the solution is obtained via the least squares [41]. To this aim, the update correlation is expanded by the linear combination of some basis functions $\Phi_q(\varphi)$, $q=1,\cdots,Q$ as

$$\delta r(\varphi)=\sum_{q=1}^{Q}a_q\Phi_q(\varphi). \tag{40}$$

Hence, the problem turns into finding unknown coefficients of (40). For a set of grid points $\varphi^1,\cdots,\varphi^P$, the unknown coefficients are determined by minimizing the sum of squares at n^{th} iteration, *i.e.,*

$$\sum_{p=1}^{P}\left|\mathcal{D}'(r_n,u_{0_n},\psi_{0_n})\sum_{q=1}^{Q}a_q\Phi_q(\varphi^p)-\Delta u_\infty\right|^2. \tag{41}$$

The whole procedure is summarized as follows:

(i). Choose a closed curve for the initial guess $\rho=r_0(\varphi)$
(ii). Obtain the surface currents of the closed curve and thus the far-field pattern using (16) and (34), respectively.
(iii). Solve (36) and (38) in the sense of least squares (40)-(41) for the updated correlation function δr_0
(iv). Obtain the new surface profile via (39)
(v). Repeat (ii)-(iv) for n times ($n>1$) such that $r_{n+1}=r_n+\delta r_n$.
(vi). Break the loop, if $\|\delta r_n\|\leq\xi$

Here, the crucial part of the whole framework is the Frechet derivative part, which is for a mapping from a domain of functions [42]. For the sake of simplicity, one may consider the Frechet derivative $\mathcal{D}'(r_0;u_{1_0},\psi_{1_0})\delta r_0:=\mathcal{D}_0'$ as the superposition of two operators

$$\mathcal{D}_0'=\mathcal{F}_{\mathcal{D}}'(r_0;\psi_{1_0})\delta r_0+\mathcal{F}_{\mathcal{N}}'(r_0;u_{1_0})\delta r_0 \tag{42}$$

where the Frechet operators are:

$$\begin{aligned}\mathcal{F}_{\mathcal{D}}'(r_0;\psi_{1_0})\delta r_0=&-\gamma\int_0^{2\pi}ik\cos\big(\varphi_s-\varphi'\big)\\&e^{-ikr_0(\varphi')\cos(\varphi_s-\varphi')}\psi_{1_0}(\varphi')\\&\sqrt{r(\varphi')^2+r'(\varphi')^2}\,\delta r_0 d\varphi',\end{aligned} \tag{43}$$

$$\begin{aligned}\mathcal{F}_{\mathcal{N}}'(r_0;u_{1_0})\delta r_0=&-\gamma\int_0^{2\pi}\Bigg(ik\cos\big(\varphi_s-\varphi'\big)\\&\kappa(r_0,\varphi',\varphi_s)u_{1_0}(\varphi')\\&+\frac{\partial\kappa(r_0,\varphi',\varphi_s)}{\partial r_0}u_{1_0}(\varphi')\Bigg)\\&e^{-ikr_0(\varphi')\cos(\varphi_s-\varphi')}\,\delta r_0 d\varphi',\end{aligned} \tag{44}$$

and κ function

$$\kappa(r_0,\varphi,\varphi_s)=r_0\cos(\varphi_s-\varphi)-r_0'\sin(\varphi_s-\varphi) \tag{45}$$

is basically the result of $\hat{k}_s\cdot\hat{\nu}$.

5. Numerical results and discussion

The section is reserved to demonstrate the feasibility of the proposed inverse framework. For all considered scattering scenarios, the operating frequency is 300MHz so that the wavelength in free-space $\lambda_0=1$m. For all numerical examples, the predetermined threshold is $\xi=0.07$. Except for

one example, the far-field pattern is assumed to be known at 64 points equally distributed around the unit circle. For the expansion of the unknown updated correlation function with some basis functions, $\Phi_q(\varphi) = e^{-iq\varphi}$, $q = 0, \pm 1, \cdots \pm Q$. To verify the success of the reconstructions quantitatively, an ℓ_2-norm based error is defined precisely

$$err(\%) = \frac{\|r(\varphi) - r_n(\varphi)\|}{\|r(\varphi)\|} \times 100, \qquad (46)$$

where $r(\varphi)$ and $r_n(\varphi)$ represent the actual and the reconstructed surfaces, respectively.

The first example aimed to put forth the effect of the penetrability of the object on the inverse algorithm. To this aim, a kite-like object is considered for reconstruction, considering both PEC and dielectric cases. The unknown kite-like surface is a radial function

$$r(\varphi) = 1.5\big(1 + 0.15\cos(3\varphi)\big). \qquad (47)$$

For the dielectric case, the constitutive EM parameters are $\varepsilon_1 = 4\varepsilon_0$ and $\sigma = 10^{-5}$ (S/m). For both PEC and dielectric cases, the region is illuminated by 7 incident illuminations simultaneously, for which the angles of incidence are selected in the range: $0° : \Delta\varphi_i : 330°$ with the $\Delta\varphi_i = 55°$ angular increments. The reconstructions and the actual surface for PEC and Dielectric scenarios are shown in Fig. 5 and Fig. 6, respectively.

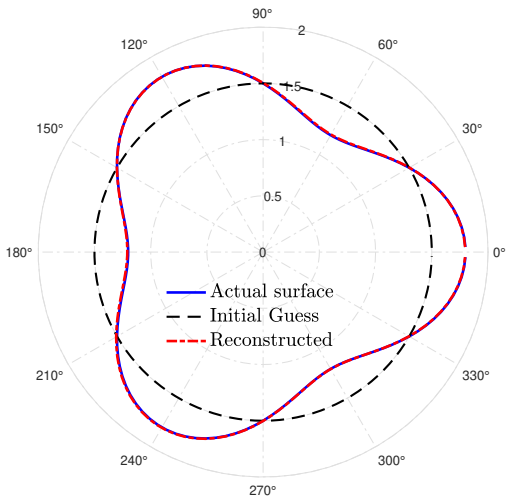

Figure 5. Reconstruction of the surface defined in (47) for PEC case.

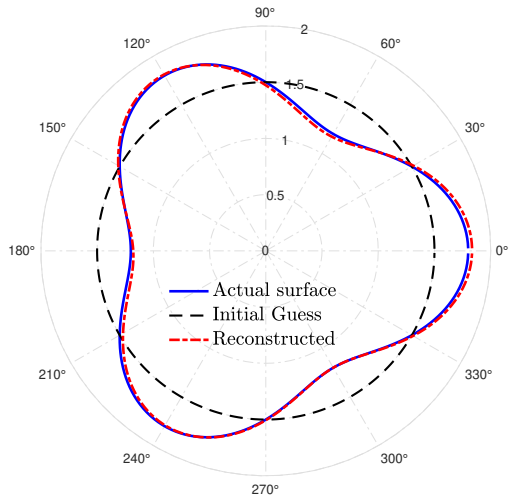

Figure 6. Reconstruction of the surface defined in (47) for Dielectric (penetrable) case.

It is worth noting that for the PEC case, the far-field pattern of the scattered field is represented with a single layer potential as shown in [32] in detail. Accordingly, for the Frechet derivative of the PEC case, (43) should be taken into consideration. As illustrated in the figure, a cross-section of an infinitely long cylinder with a radius $1.5\lambda_1$ is considered as the initial guess for both cases. Moreover, both cases' stopping criteria are $\|\delta r\| \leq \xi = 0.07$. Accordingly, the needed 16 iteration is for the PEC case, and the 28 iteration is for the dielectric case. To visualize the expected decreasing tendency of the $\|\delta r\|$ for each new iteration, Fig. 7 shows $\|\delta r\|$ versus the number of iterations for the dielectric case.

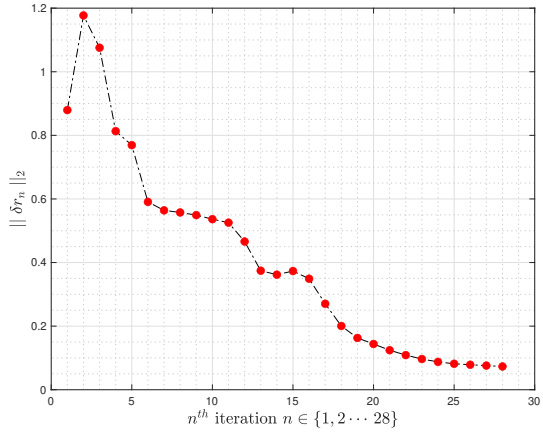

Figure 7. $\|\delta r_n\|$ vs. iterations.

In addition, the reconstruction of PEC is better than the dielectric case qualitatively and quantitatively. This is mostly because the PEC case has no penetrated field to the second region. Hence, a more powerful scattered field contains more information for the scatterer, leading to better

reconstructions. The quantitative errors for both cases are $err(\%) = 0.31\%$ and $err(\%) = 1.37\%$, respectively, for PEC and dielectric cases.

The next analysis covers the algorithm's sensitivity to the constitutive parameters of the dielectric object, *i.e.,* ε_r and σ. Accordingly, the response of the algorithm is tested for higher and lower dielectric permittivity and conductivity values. In this regard, "4− leaf" shape boundary curve is assumed to be unknown, and it is reconstructed for different ε_r and σ values. The considered "leaf-shaped" radial function is defined as

$$r(\varphi) = 1.3\big(1 + 0.15\cos(4\varphi)\big) \tag{48}$$

First, the objective is to observe the dielectric dependency of the iterative inverse reconstruction algorithm. In order to notice the sensitivity to the dielectric permittivity, the algorithm is run for different ε_r values for a fixed conductivity $\sigma = 10^{-5}$ (S/m). Within this context, the dielectric permittivity range is taken into account $\varepsilon_r \in [2, 10]$. Hence, the dielectric permittivities are defined in a wide range, from very penetrable cases to high levels. For all reconstructions, run for different ε_r, the circle with radius $1.5\lambda_1$ is considered for the initial guess. The obtained quantitative errors of the reconstructions for different dielectric permittivity values are shown in Fig. 8.

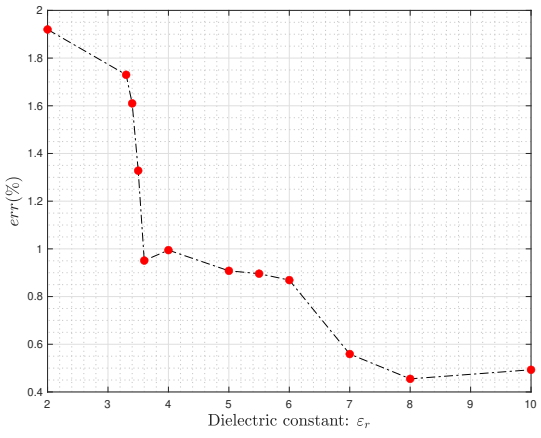

Figure 8. Error: $err(\%)$ vs. dielectric constant: ε_r

As shown, the bigger contrast between free space and the dielectric object yields better reconstructions quantitatively. It is worth noting that if $\varepsilon_r < 2$, it becomes impossible to obtain accurate reconstructions. Furthermore, $\varepsilon_r > 10$ yields higher computational cost as the inversion algorithm needs a direct solver whose unknown is directly related to the dielectric permittivity ε_r. A similar analysis was also carried out to observe the conductivity sensitivity. To this aim, $\varepsilon_r = 2$ is fixed and the conductivity varies in the range $\sigma \in [5 \times 10^{-7}, 10^{-2}]$ (S/m). The algorithm's errors for different conductivity values are shown in Fig. 9

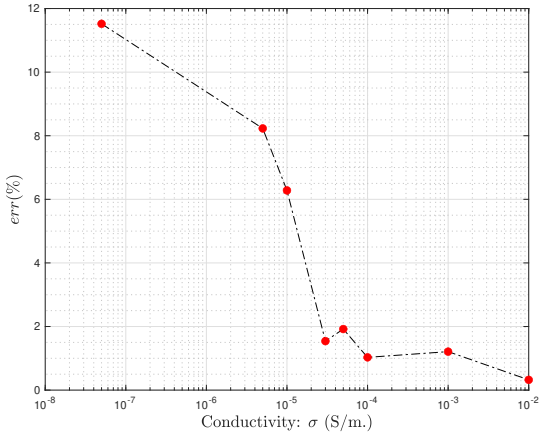

Figure 9. Error: $err(\%)$ vs. conductivity σ (S/m)

Accordingly, the higher conductivity yields better reconstructions such that for $\sigma = 10^{-2}$, the error $err < 0.4\%$. However, such a high conductivity yields a huge loss, so the unknown object can almost turn into PEC rather than a penetrable object. Fig. 10 shows the worst and the best cases together to demonstrate reconstructions visually.

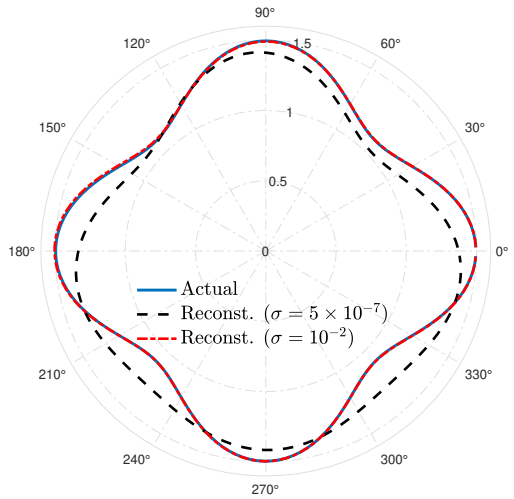

Figure 10. Reconstructions for the highest and the lowest conductivity values

Noting that the region is illuminated for 12 incident plane waves simultaneously where the angles of incidence are defined as $0° : \Delta\varphi_i : 330°$ with the $\Delta\varphi_i = 30°$ angular increments. Again, the

circle with the radius $1.5\lambda_1$ is considered the initial guess. For all analyses conducted to obtain the sensitivity to the constitutive parameters, 19 exponential-type basis functions are applied in the sense of least squares.

The next analysis covers the algorithm's sensitivity against noise. For this purpose, a synthetic noise is added to the far-field pattern. The noisy scattered field is defined as $\tilde{u}_\infty = u_\infty + n_\ell |u_\infty| e^{i2\pi r_d}$, where n_ℓ is the noise-level and r_d is the random number in the interval $0 < r_d < 1$. The bean-shaped object is considered for the noise analyses. It is defined as

$$r(\varphi) = 0.8\frac{1 + 0.85\cos\left(\varphi + \frac{\pi}{4}\right) + 0.05\sin\left(2\varphi + \frac{\pi}{4}\right)}{1 + 0.5\cos\left(\varphi + \frac{\pi}{4}\right)}. \tag{49}$$

In regards to the scattering scenario, $\varepsilon_r = 4$ and $\sigma = 10^{-5}$ (S/m), and the number of 6 incident illuminations is applied simultaneously, where $\varphi_i^n = \{0°, 60°, 120°, 180°, 240°, 300°\}$. Fig. 11 shows the obtained quantitative errors for different noise levels.

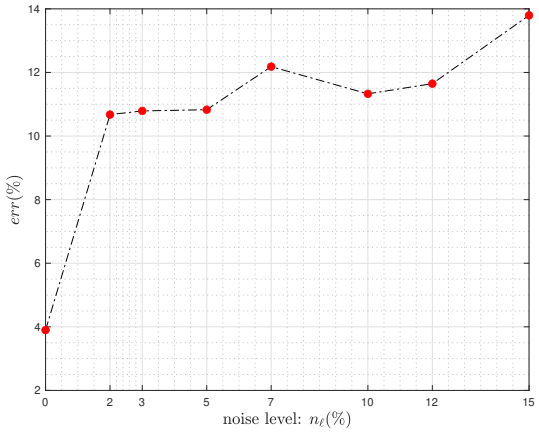

Figure 11. Error: $err(\%)$ vs. noise level: $n_\ell(\%)$

Accordingly, the algorithm is sensitive to the noise such that $n_\ell(\%) \leq 10\%$ for satisfactory reconstructions. The reconstructions for the noise-free case and with the highest noise level are shown in Fig. 12

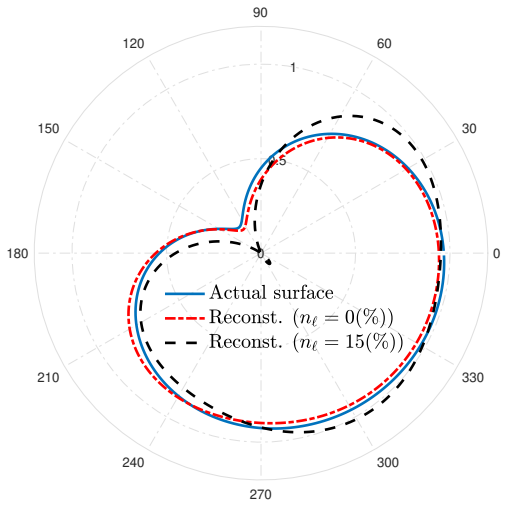

Figure 12. Reconstruction of the bean-shaped object for the noise-free and the highest noise level

The following example investigates the sensitivity of the reconstructions to the amount of scattered field data. Let #MP denote the number of measurement points. It is worth to remind that, up to this example, #MP = 64. To this aim, a 5-leaf shape is reconstructed for different numbers of scattered field data. The inaccessible 5-leaf shape is defined as

$$r(\varphi) = 1.3\big(1 + 0.15\cos(5\varphi)\big) \tag{50}$$

For the sensitivity analysis to the number of scattered field data, the remaining parameters are kept constant such as the number of incident fields is 11, precisely defined in the range $\varphi_i = 0° : 30° : 300°$, the penetrable medium parameters are $\varepsilon_r = 4$, $\sigma = 10^{-5}$ S/m and the number of applied exponential basis functions are 27. The obtained error vs the amount of the measured field data is given in Fig. 13

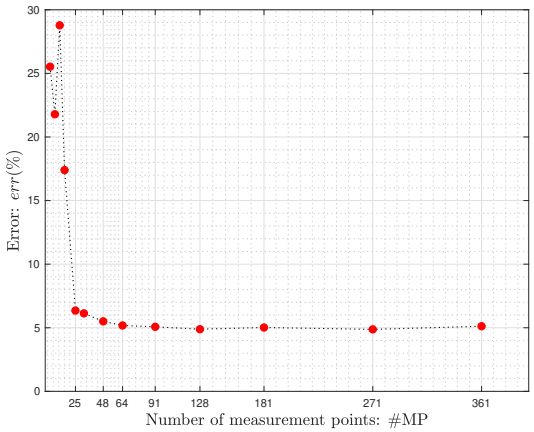

Figure 13. Error: $err(\%)$ vs. the number of measurement points: #MP

Accordingly, insufficient reconstructions observed for#MP < 25. For an accurate result, #MP $\geq$

25. As shown in Fig. 13, the error remains around 5% such that the differences between the reconstructions cannot be distinguished with the naked eye. To visualize this, the unsuccessful reconstructions obtained for #MP = 8, #MP = 16 and the satisfactory result of #MP = 32 are shown in Fig. 14

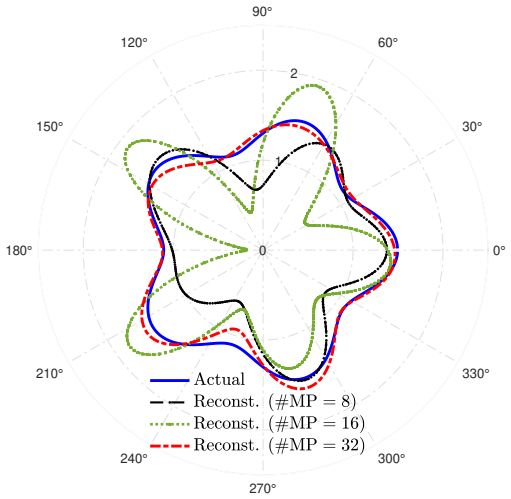

Figure 14. Reconstructions for different #MP values

The next analysis is carried out to emphasize the significance of multi-illumination. For this purpose, a potato-shaped curved object is considered. It is defined as a radial function

$$r(\varphi) = 4\sqrt{\left(\tfrac{1}{4} + \tfrac{3}{40}\cos(2\varphi)\right)^2 + \left(\tfrac{1}{4} + \tfrac{3}{100}\cos(3\varphi)\right)^2}. \tag{51}$$

In the first case, the object is illuminated with a single incident plane wave with the angle of incidence $\varphi_i = 0°$. The result is shown in Fig. 15

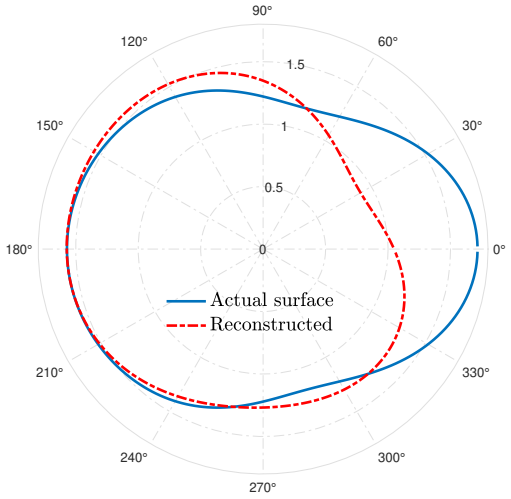

Figure 15. Reconstruction of the potato-shaped object with a single incident illumination

As illustrated, the reconstruction is unsatisfactory as the shadow region predominates inversion [24,33,43]. To overcome this, the same object is recovered for the superposition of 4 incident plane waves. The angles of incidence are $\varphi_i^n = \{-30, 30, 150, 210\}$, for $n = \{1, 2, 3, 4\}$. The satisfactory reconstruction for the multi-incidence is illustrated in Fig. 16

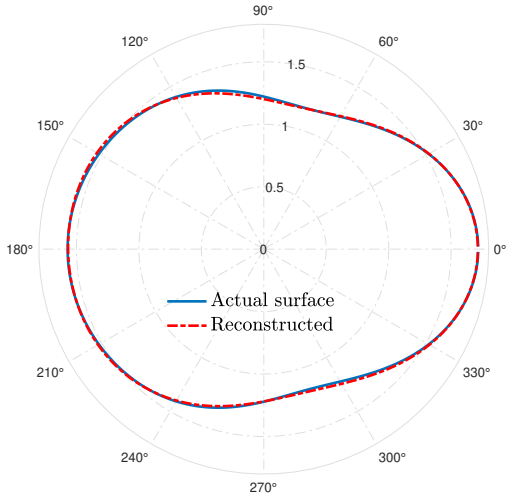

Figure 16. Reconstruction of the potato-shaped object with superposition of multi-incident illumination

Noting that, for both multi and single-illumination cases of potato shape objects, $\varepsilon_r = 4$ and $\sigma = 10^{-5}$ (S/m) and there are 13 exponential basis functions were utilized. Actually, the superposition of multi-incidence illumination is one of the essential factors for satisfactory reconstructions. To underline this, all 2D shapes reconstructed so far have been reconstructed again by considering different numbers of incident illumination in the following analysis. The error for different number of illuminations are shown in Fig. 17

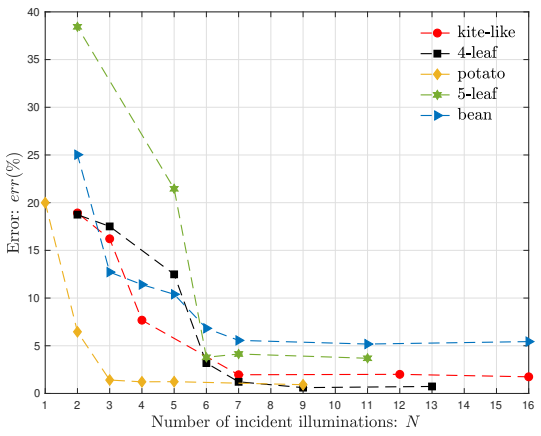

Figure 17. Error: $err(\%)$ vs. number of multi-incidence illumination: N

Table 1. Parameters for the superposition of the multi-incident illumination

$r(\varphi)$	Angels of incidence: $\varphi_i^1 : \Delta\varphi : \varphi_i^N$	increments: $\Delta\varphi$ (Deg.)	number of incident field in superposition: N
3-leaf	$0° : \Delta\varphi : 330°$	{22, 30, 55, 110, 165, 330}	{2, 3, 4, 7, 12, 16}
4-leaf	$0° : \Delta\varphi : 360°$	{30, 45, 60, 72, 90, 180, 360}	{2, 3, 5, 6, 7, 9, 13}
5-leaf	$0° : \Delta\varphi : 300°$	{20, 30, 45, 60, 75, 90, 150, 300}	{2, 3, 4, 5, 6, 7, 11, 16}
potato	$-30° : \Delta\varphi : 210°$	{30, 60, 80, 120, 240, }	{1, 2, 3, 4, 5, 9} (Single illumination at 0°)

As shown in Fig. 17, there are no satisfactory reconstructions for a single or double illumination. As expected, the error starts to decrease for increasing the number of illuminations, and after a specific number, it remains almost constant for each specific reconstruction. There is no certain value because it differs for every shapes. However, one can conclude that at least 2 incidence illumination should be considered even for a simple object (like the potato). The details of the analysis are given in Table 1. The table states the incident fields angles, given in (4), by defining $\varphi_i^1 : \Delta\varphi : \varphi_i^N$. Here, φ_i^1 and φ_i^N are the initial and the final angles of the illumination, and $\Delta\varphi$ denotes the increments.

The next example shows the reconstruction of a peanut-shaped object for the same constitutive EM parameters with different initial guessed surfaces. The object is defined with a radial function

$$r(\varphi) = 0.7\sqrt{\left(0.2\cos^2(\varphi) + \sin^2(\varphi)\right)}. \qquad (52)$$

Two incident illuminations were utilized with $\varphi_i = \{90°, 270°\}$. In this example, the reconstruction carried out for considering both a circular cylinder with a radius $0.6\lambda_1$ and an ellipse defined as:

$$r_0(\varphi) = \frac{ab}{\sqrt{\left(a\cos^2(\varphi) + b\sin^2(\varphi)\right)}}, \qquad (53)$$

where $a = 0.6\lambda_1$ and $b = 0.4\lambda_1$. Since the elliptical initial guess is more similar to the actual peanut-shaped object, one may consider that using an elliptical cylinder as the initial guess would lead to a better reconstruction. However, both qualitatively and quantitatively, the difference between reconstructions is almost negligible. It is obtained $err = 3.73\%$ with the circular cylinder initial guess and $err = 3.61\%$ for the case of the elliptical cylinder. The only difference is that it requires 7 iterations for the elliptical case, whereas it costs 11 for the circular initial guess. Thus, the method is stable and robust. Fig. 18 demonstrates the reconstruction, the elliptical initial guess, and the actual surface.

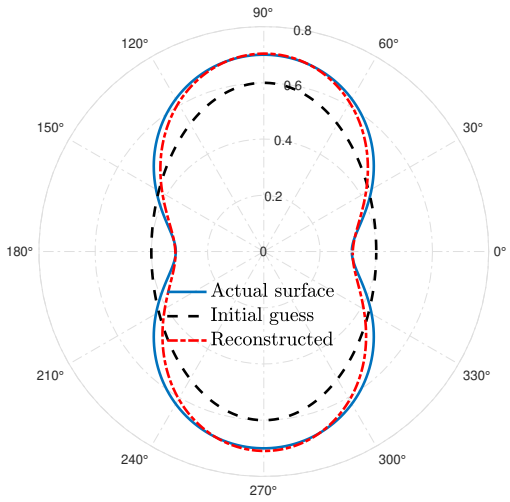

Figure 18. Reconstruction of the peanut-shaped object with the initial guess

For the peanut reconstruction cases, $n_\ell = 2\%$ noise is applied for all the simulations, and 13 exponential functions are applied in the least square sense.

6. Conclusion

A regularized and linearized iterative framework is presented to recover the shape of inaccessible 2-dimensional dielectric objects. The proposed framework utilizes the far-field pattern of the scattered field data for this aim. The inversion is done in accordance with the boundary integral representation of the far-field pattern considering the combination of the double and single-layer potentials. The problem is inherently ill-posed and nonlinear. Within this context, the Newton-type iterative linearization technique is applied, and it is regularized via Tikhonov in the sense of the least squares approach. To overcome the adverse effect of the shadow region on the imaging process, the superposition of the multi-incident wave

is taken into account. Accordingly, robust and fast inversion is achieved with a very low computational cost. The feasibility of the proposed framework and its validation limits are asserted via various scattering scenarios.

The algorithm may be extended for three-dimensional imaging problems in the acoustic case, as it still requires a scalar solution to the wave equations. However, the EM case must be reformulated, as the scattering problem needs a vectorial solution. The validation limits can be enlarged with hybrid approaches generated with deep learning techniques. All these issues are left as future works.

Appendix

$\overline{I}_{die}$ and $\overline{V}_{die}$ are vectors with size $2N \times 1$ whose elements are precisely

$$\overline{I}_{die} = \left[u_0\, u_1 \cdots u_N\, \psi_0\, \psi_1\, \cdots \psi_N \right]^T, \qquad \text{(A.1)}$$

and tested incident fields with Dirac-delta function yields:

$$\overline{V}_{die} = \left[u^i(\varphi_1)\; u^i(\varphi_2) \cdots u^i(\varphi_N) \underbrace{0\;\; 0 \cdots 0}_{N} \right]^T. \qquad \text{(A.2)}$$

Finally, the impedance matrix has a size of $2N \times 2N$, which is composed of 4 sub-matrices, each of which has a size $N \times N$:

$$\overline{Z}_{die} = \begin{bmatrix} \overline{Z^{1u}} & \overline{Z^{1\psi}} \\ \overline{Z^{2u}} & \overline{Z^{2\psi}} \end{bmatrix}. \qquad \text{(A.3)}$$

The elements of $\overline{Z^{j\psi}}$ $(j = \{1, 2\})$ are $N \times N$ are given as

$$Z^{j\psi}_{mn} = \Delta\varphi_n \begin{cases} G_j(\boldsymbol{r_m}; \boldsymbol{r_n}) & m \neq n \\ \frac{i}{4}\left[1 + i\frac{2}{\pi} \ln\left(\frac{\gamma k_0}{4e} \Delta\varphi_n \right) \right] & m = n. \end{cases} \qquad \text{(A.4)}$$

Here, $\gamma = 1.78107$. The sub-matrix $\overline{Z^{1u}}$ has the elements

$$Z^{1u}_{mn} = \Delta\varphi_n \begin{cases} -K_0(\boldsymbol{r_m}; \boldsymbol{r_n}) & \text{for } m \neq n \\ \frac{1}{2} & \text{for } m = n. \end{cases} \qquad \text{(A.5)}$$

$\overline{Z^{2u}}$ has the same format with (A.5) taking the wavenumber k_1 instead of k_0 into account. Moreover, the diagonal elements of $\overline{Z^{2u}} = -1/2$ in accordance with the (16).

References

[1] Tuz, M.(2017). Boundary values for an eigenvalue problem with a singular potential. *An International Journal of Optimization and Control: Theories & Applications (IJOCTA)*, 7(3), 293–300. https://doi.org/10.11121/ijocta.01.2017.00507

[2] Aydin, C., & Tezer, M. (2019). the DRBEM solution of cauchy MHD duct flow with a slipping and variably conducting wall using the well-posed iteration. (2019) *An International Journal of Optimization and Control: Theories & Applications (IJOCTA)*, 9(3), 76–85. https://doi.org/10.11121/ijocta.01.2019.00677

[3] Karatas Akgul, E. (2018). Reproducing kernel Hilbert space method for solutions of a coefficient inverse problem for the kinetic equation. *An International Journal of Optimization and Control: Theories & Applications (IJOCTA)*, 8(2), 141–151. https://doi.org/10.11121/ijocta.01.2018.00568

[4] Ozmen, A. (2022). Multi-objective regression modeling for natural gas prediction with ridge regression and CMARS. *An International Journal of Optimization and Control: Theories & Applications (IJOCTA)*, 12(1), 56–65. https://doi.org/10.11121/ijocta.2022.1084

[5] Acil, M., & Konuralp, A. (2021). Reconstruction of potential function in inverse Sturm-Liouville problem via partial data. *An International Journal of Optimization and Control: Theories & Applications (IJOCTA)*, 11(2), 186–198. https://doi.org/10.11121/ijocta.01.2021.001090

[6] Sefer, A. (2022). Locally perturbed inaccessible rough surface profile reconstruction via phaseless scattered field data. *IEEE Transactions on Geoscience and Remote Sensing,*, 60, 1–8. https://doi.org/10.1109/TGRS.2021.3105257

[7] Bilgin, E., Cayoren, M., Joof, S., Cansiz, G., Yilmaz, T., & Akduman, I. (2022). Single-slice microwave imaging of breast cancer by reverse time migration. *Medical Physics*, 49(10), 599–6608. https://doi.org/10.1002/mp.15917

[8] Dogu, S., Akinci, M. N., & Gose, E. (2022). Experimental moving target imaging in a nonanechoic environment with linear sampling method. *IEEE Geoscience and Remote Sensing Letters*, 18(3), 441–445. https://doi.org/10.1109/LGRS.2020.2976594

[9] Colton, D., & Kress, R. Smith, G. (2019). Ill-posed Problems. In: P. Holmes, S.S. Antman, K. Sreenivasan eds. *Inverse Acoustic and Electromagnetic Scattering Theory.* Wiley - 3rd ed. 4th ed. Springer, London. 95–118.

https://doi.org/10.1007/978-1-4614-4942-3_4

[10] Ghazi, F. F., & Tawfiq, L. N. M. (2024). Design optimal neural network based on new LM training algorithm for solving 3D - PDEs. *An International Journal of Optimization and Control: Theories & Applications (IJOCTA)*, 14(3), 249–250. https://doi.org/10.11121/ijocta.1519

[11] Ozmen, A. (2022). Multi-objective regression modeling for natural gas prediction with ridge regression and CMARS. *An International Journal of Optimization and Control: Theories & Applications (IJOCTA)*, 12(1), 56–65. https://doi.org/10.11121/ijocta.2022.1084

[12] Kumar A., Kumar, M., & Goswami, P.(2024). Numerical solution of coupled system of Emden-Fowler equations using artificial neural network technique. *An International Journal of Optimization and Control: Theories & Applications (IJOCTA)*, 14(1), 62–73. https://doi.org/10.11121/ijocta.1424

[13] Salucci, M., Arrebola, M., Shan, T., & Li, M. (2022). New frontiers in real-time inverse scattering and electromagnetic imaging. *IEEE Transactions on Antennas and Propagation*, 70(8), 6349–6364. https://doi.org/10.1109/TAP.2022.3177556

[14] Desmal, A. (2022). A trained iterative shrinkage approach based on born iterative method for electromagnetic imaging. *IEEE Transactions on Antennas and Propagation*, 70(11), 4991–4999. https://doi.org/10.1109/TMTT.2022.3205650

[15] Desmal, A., & Alsaei, J. (2024). Multifrequency trained projection nonlinear framework for electromagnetic imaging with contrast-source landweber-kaczmarz. *IEEE Geoscience and Remote Sensing Letters*, 21, 1–5, Art no. 3002505. https://doi.org/10.1109/LGRS.2024.3397694

[16] Yao, H. M., Sha, W.E.I.,& Jiang,L. (2019). Two-step enhanced deep learning approach for electromagnetic inverse scattering problems. *IEEE Antennas and Wireless Propagation Letters*, 18(11), 2254–2258. https://doi.org/10.1109/LAWP.2019.2925578

[17] Aydin, I., Guven, B., Sefer, A., & Yapar, A. (2022). CNN-based deep learning architecture for electromagnetic imaging of rough surface profiles. *IEEE Transactions on Antennas and Propagation*, 70(10), 9752–9763. https://doi.org/10.1109/TAP.2022.3177493

[18] Song, L., Kuang, L., Han, Y., Wang, Y., & Liu, Q. H. (2018). Inversion of rough surface parameters from SAR images using simulation-trained convolutional neural networks. *IEEE Geoscience and Remote Sensing Letters*, 15(7), 1130–1134. https://doi.org/10.1109/LGRS.2018.2822821

[19] Aydin, I., Guven, B., Sefer, A., & Yapar, A. (2022). Recovery of impenetrable rough surface profiles via CNN-based deep learning architecture. *International Journal of Remote Sensing*, 43(15-16), 5658–5685. https://doi.org/10.1080/01431161.2022.2105177

[20] Wang, X., Zhu, J., Song, M., & Wu, W. (2022). Fourier method for reconstructing elastic body force from the coupled-wave field. *Inverse Problems and Imaging*, 16(2), 325–340. https://doi.org/10.3934/ipi.2021052

[21] Sefer, A., Yapar, A., & Yelkenci, T. (2024). Imaging of rough surfaces by RTM method. *IEEE Transactions on Geoscience and Remote Sensing*, 62, 1–12, Art no. 2003312, doi: 10.1109/TGRS.2024.3374972 https://doi.org/10.1109/TGRS.2024.3374972

[22] Sefer, A., & Yapar, A., (2022). Inverse scattering by perfectly electric conducting (PEC) rough surfaces: An equivalent model with line sources. *IEEE Transactions on Geoscience and Remote Sensing*, 60, 1–9, Art no. 2007109. https://doi.org/10.1109/TGRS.2022.3210657

[23] Blasten, E. L.K., & Liu, H. (2021). Scattering by curvatures, radiationless sources, transmission eigenfunctions, and inverse scattering problems. *SIAM Journal on Mathematical Analysis*, 53(4), 3801–3837. https://doi.org/10.1137/20M1384002

[24] Guo, Y., & Zhang, D. (2011). An optimization method for acoustic inverse obstacle scattering problems with multiple incident waves. *Inverse Problems in Science and Engineering*, 19(4), 461–484. https://doi.org/10.1080/17415977.2010.518286

[25] Bao, G., Li, P., Lin, J., & Triki, F. (2015). Inverse scattering problems with multi-frequencies. *Inverse Problems*, 31, 093001. https://doi.org/10.1088/0266-5611/31/9/093001

[26] Altundag, A., & Kress, R. (2012). On a two dimensional inverse scattering problem for a dielectric. *Applicable Analysis*, 91(4), 757-771. https://doi.org/10.1080/00036811.2011.619981

[27] Qu, F., Yang, J., & Zhang, H. (2019). shape reconstruction in inverse scattering by an inhomogeneous cavity with internal measurement. *SIAM Journal on Imaging Sciences*, 12(2), 788–808. https://doi.org/10.1137/18M1232401

[28] Cheng, Z., & Dong, H. (2023). Uniqueness and reconstruction method for inverse elastic wave scattering with phaseless data. *Inverse Problems and Imaging*, 18(12), 406–433.

[29] Borges, C., Gillman, A., & Greengard, L. (2017). High resolution inverse scattering in two dimensions using recursive linearization. *SIAM Journal on Imaging Sciences*, 10(2), 641–664. https://doi.org/10.1137/16M1093562

[30] Borges, C., Rachh, M., & Greengard, L. (2023). On the robustness of inverse scattering for penetrable, homogeneous objects with complicated boundary. *Inverse Problems*, 39(3), 035004. https://doi.org/10.1088/1361-6420/acb2ec

[31] Sefer, A., & Yapar, A. (2021). An iterative algorithm for imaging of rough surfaces separating two dielectric media. *IEEE Transactions on Geoscience and Remote Sensing*, 59(2), 1041–1051. https://doi.org/10.1109/TGRS.2020.2997637

[32] Johansson, T., & Sleeman, B. D. (2007). Reconstruction of an acoustically sound-soft obstacle from one incident field and the far-field pattern. *IMA Journal of Applied Mathematics*, 72(1), 96–112. https://doi.org/10.1093/imamat/hxl026

[33] Zinn, A. (1989). On an optimization method for the full and the limited-aperture problem in inverse acoustic scattering for a sound-soft obstacle. *Inverse Problems*, 5(2), 239–253. https://doi.org/10.1088/0266-5611/5/2/009

[34] Tsang, L., Kong, J. A., Ding, K.-H., & Ao, C. O. (2001). *Scattering of Electromagnetic Waves, Numerical Simulations*, 1st ed. Wiley, NY USA. https://doi.org/10.1002/0471224308

[35] Bourlier, C., Pinel, N., & Kubicke, G. (2013). Validation of the Method of Moments for a Single Scatterer. In: Joseph Saillard, ed. *Method of Moments for 2D Scattering Problems*. Wiley - ISTE, NY USA, 31–72. https://doi.org/10.1002/9781118648674.ch2

[36] Abramowitz, M., & Stegun, A. (1964). *Handbook of Mathematical Functions with Formulas, Graphs, and Mathematical Tables*, 1st ed. Dover, NY USA.

[37] Bourlier, C., Pinel, N., & Kubicke, G. (2013). Integral Equations for a Single Scatterer: Method of Moments and Rough Surfaces. In: Joseph Saillard, ed. *Method of Moments for 2D Scattering Problems*. Wiley - ISTE, NY USA, 1–30. https://doi.org/10.1002/9781118648674.ch1

[38] Ishimaru, A. (2017). Radiation from Apertures and Beam Waves. In: Tariq Samad, ed. *Electromagnetic Wave Propagation Radiation and Scattering*. 2nd ed. IEEE Press, Piscataway, NJ. 169–199. https://doi.org/10.1002/9781119079699.ch6

[39] Altundag, A (2012). *On a Two-Dimensional Inverse Scattering Problem for a Dielectric*. PhD Thesis. Georg-August-Universität zu Göttingen.

[40] Fan, J., & Pan, J. (2004). Inexact Levenberg-Marquardt method for nonlinear equations. *Discrete and Continuous Dynamical Systems Series B*, 4(4), 1223–1232. https://doi.org/10.3934/dcdsb.2004.4.1223

[41] Sefer, A. (2022). Optimization of inverse problems involving surface reconstruction: Least-square application. *Proceedings of the 3rd AT-AP-RASC*. 1–4. https://doi.org/10.23919/AT-AP-RASC54737.2022.9814221

[42] Potthast, R. (1994). Frechet differentiability of boundary integral operators in inverse acoustic scattering. *Inverse Problems*, 10(2), 431–447. https://doi.org/10.1088/0266-5611/10/2/016

[43] Kirsch, A., & Kress, R. (1988). Two methods for solving the inverse acoustic scattering problem. *Inverse Problems*, 4(3), 749–770. https://doi.org/10.1088/0266-5611/4/3/013

Ahmet Sefer *received a B.Sc. in electrical and electronics engineering from Bilkent University, Ankara, Turkey, in 2010 and a Ph.D. from the Graduate School of Istanbul Technical University, Istanbul, Turkey, in 2021. Since September 2021, he has been an Assistant Professor with the Department of Electrical and Electronics Engineering at FMV Isik University, Istanbul, Turkey. Since March 2023, he has been a postdoctoral fellow at King Abdullah University of Science and Technology (KAUST), Saudi Arabia. Dr. Sefer received the Leopold B. Felsen Excellence in Electrodynamics Award from Leopold B. Felsen Fund, in 2020. He is currently a member of the IEEE Antennas and Propagation Society and IEEE Geoscience and Remote Sensing Society. He has been Chair of IEEE Antennas and Propagation Society-Istanbul Chapter. His research interests include electromagnetic theory, direct and inverse scattering problems, integral equations, and numerical techniques.*

https://orcid.org/0000-0001-5168-4367

An International Journal of Optimization and Control: Theories & Applications (http://www.ijocta.org)